

Plasma effects on gravitational lensing and shadow observables of a Kerr-like black hole in a dark matter halo

Connor McMillin,^{1,*} Zhichen Guan,^{1,†} Owen Gartlan,^{1,‡} Lotus Liu,^{2,§} Leo Rodriguez,^{1,3,¶} and Shanshan Rodriguez^{1,3,4,**}

¹*Department of Physics, Grinnell College, Grinnell, IA 50112*

²*Department of Physics, University of Chicago, Chicago, IL 60637*

³*Department of Physics, Worcester Polytechnic Institute, Worcester, MA 01609*

⁴*Center for Astrophysics, Harvard & Smithsonian, Cambridge, MA 02138*

(Dated: March 13, 2026)

Plasma, as a medium around the black hole for light propagation, is known to visibly alter the shape of its shadow and the observables, which could impact the interpretation of the Event Horizon Telescope results. In this study, we examine how dark matter and non-magnetized, pressureless plasma influence the shadow of a Kerr-like black hole. We analyze the null-geodesics in the presence of both homogeneous and inhomogeneous plasma profiles and show how their influence on photon orbits affects the resulting black hole shadow. Our findings indicate that increasing the black hole's spin generally enlarges both the shadow radius and deformation. Additionally, the viewing angle decreases the shadow radius while reducing deformation as the observer moves farther from the equatorial plane. For this model, astrophysically reasonable amounts of dark matter show no significant impact on the photon trajectories. However, we observe that increasing plasma density increases both the shadow radius and deformation for homogeneous plasma, while it decreases them for inhomogeneous plasma. The emission rate also depends significantly on the model of plasma chosen, with homogeneous plasma causing significantly more emission as plasma strength increases. We also study the constraints obtained from comparing theoretical shadow radii with EHT observations of M87* and Sgr A*, which allows us to infer reasonable plasma distribution properties and frequencies in our theoretical model.

PACS numbers: 11.25.Hf, 04.60.-m, 04.70.-s

I. INTRODUCTION

Black-hole shadows and strong-field gravitational lensing have become powerful observational tools for probing gravity and the near-horizon environment of compact objects. The first horizon-scale image of the supermassive black hole in M87* released by the Event Horizon Telescope (EHT) marked a major milestone, revealing a bright, asymmetric ring surrounding a central brightness depression whose angular scale is consistent with the characteristic photon-orbit size predicted by general relativity [1]. This result demonstrated that shadow observables can be measured with sufficient precision to test theoretical models. The subsequent EHT image of Sgr A* extended these tests to our Galactic center, despite the additional challenges posed by rapid source variability and scattering effects [2]. These observations motivate continued theoretical efforts to understand how both spacetime geometry and astrophysical environments influence gravitational lensing and the apparent size and shape of black-hole shadows [3–5]. In realistic environments, however, light does not propagate in a vacuum: plasma around the black hole introduces refraction and dispersion, so the apparent shadow and lensing observables become frequency dependent [6]. A widely used starting point

is the Hamiltonian/refractive-index formulation for photon propagation in plasma on curved spacetimes, developed in different forms for magnetized and non-magnetized media [7]. This framework underlies much of the modern literature connecting theoretical shadow/lensing predictions to astrophysical settings and to EHT-scale observations.

A substantial body of work has explored what plasma does to shadow size and deformation under a variety of models. For static, spherically symmetric spacetimes, Perlick, Tsupko, and Bisnovatyi-Kogan derived analytic expressions for the angular shadow size in a non-magnetized, pressureless plasma with general radial density profiles, and showed explicitly how the shadow radius becomes frequency dependent; they also discussed accreting (infalling) plasma examples relevant for astrophysical applications [5, 8]. For rotating spacetimes, progress accelerated once separability conditions were identified: Perlick and Tsupko showed that certain classes of plasma frequency profiles preserve separability of the Hamilton-Jacobi equation in Kerr, enabling semi-analytic characterization of photon regions and shadow boundaries [9]. The most commonly explored non-magnetized, pressureless plasma models include homogeneous plasmas and inhomogeneous power-law or radially varying density profiles [10–17]. More recent studies have considered more structured or anisotropic plasma distributions, such as Gaussian-type profiles, as well as the effects of magnetized plasma, further emphasizing that plasma modeling is essential for a realistic interpretation of shadow and lensing observables [18–21]. These results establish a fairly robust qualitative picture: plasma generically induces frequency-dependent shifts in the effective photon region, changing the shadow's “areal” size and its deformation measures, with the sign

* mcmillin@grinnell.edu

† guanzhic@grinnell.edu

‡ gartlano@grinnell.edu

§ lotusliu@uchicago.edu

¶ rodriguezl@grinnell.edu

** rodriguez@grinnell.edu; Corresponding author.

and magnitude controlled by how plasma is distributed (uniform vs. centrally concentrated vs. anisotropic), and by spin/inclination. The influence of plasma on black hole shadows has also been extensively studied in different modified gravity theories [7, 11, 22–52]. Comprehensive reviews have summarized these developments and clarified the regimes in which plasma effects are expected to be most relevant [53].

In addition, the nature of dark matter, which constitutes the dominant mass component of galaxies and 27% of the cosmic energy budget, remains a central open problem. While general relativity accurately describes its gravitational effects, it provides no insight into its microscopic origin or particle content. Astrophysical evidence, from galactic rotation curves to colliding clusters, indicates that dark matter forms extended halos in which the most massive galaxies host a central supermassive black hole [54–58]. Consequently, astrophysical black holes are not isolated systems but are embedded in matter environments. Since dark matter exhibits a weak standard model interaction, an effective way to study its astrophysical properties is to probe its gravitational influence by modifying strong-field dynamics such as particle geodesics, gravitational lensing, and shadow deformation. In particular, dark matter distributions around supermassive black holes may affect accretion, feedback, and gravitational-wave sources such as extreme and intermediate mass-ratio inspirals [59–61]. Studying black holes in realistic matter backgrounds, therefore, provides a promising avenue to probe dark matter properties and test gravity in complex astrophysical settings.

Analytical studies commonly model dark matter halos using parametric density profiles motivated by simulations and galactic dynamics, such as the Navarro-Frenk-White (NFW) profile [62, 63], Dehnen-type profiles [64–66], the Burkert model [67], and the Einasto profile, which offers greater flexibility in describing the inner halo structure and is often favored in high-resolution simulations [68, 69]. Simpler analytic profiles, such as the Hernquist model, are also frequently used as tractable approximations to galactic potentials [70, 71]. Recent work has investigated how these dark-matter distributions modify gravitational lensing and shadow properties, either through effective spacetime models or perturbative treatments, and has shown that halo parameters can lead to measurable shifts in shadow size and related observables [72–76], especially when combined with other environmental effects such as plasma [77]. These studies help disentangle how much of an observed size or deformation shift arises from dispersive photon propagation versus genuine modifications of the effective gravitational potential.

Motivated by these developments, this paper examines the combined influence of plasma and a dark-matter halo on the gravitational lensing and shadow of a Kerr-like black hole. We consider both homogeneous and inhomogeneous plasma models, adopt an Einasto profile for the dark-matter halo, and analyze how plasma frequency and halo parameters affect shadow size, deformation, and the associated energy emission rate, with particular emphasis on comparison with EHT observations of M87* and Sgr A* [1, 2].

The paper is organized as follows. In Section II, we briefly introduce the Kerr-like black hole in a dark matter halo and its horizon structure. In Section III, we introduce the plasma models used in geometrical optics around the black hole concerned. In Sections IV, V and VI, we analyze the plasma influence on photon orbits, deflection angle, black hole shadow and observables, and energy emission rate. In Section VII, we compare our results and survey the proper range for plasma frequency to match the EHT observation data from M87* and Sgr A*. We summarize our results in Section VIII. We have assumed geometrized units $\hbar = c = G = 1$ throughout this work.

II. KERR-LIKE BLACK HOLE IN A DARK MATTER HALO

For decades, computational studies have sought to model the internal structure of dark matter halos and understand how their density varies with radius. Early simulations often employed simplified analytic forms, such as the NFW profile, to describe the radial dependence of halo density [62, 63]. More recent high-resolution simulations, however, have revealed systematic deviations from these earlier models, particularly in the innermost and outermost regions of halos [78]. As a more flexible and accurate alternative, the Einasto profile is expressed as an exponential function of a power law, which allows the logarithmic slope of the halo density to vary smoothly with radius as approximately $\frac{d \ln \rho}{d \ln r} \propto r^\alpha$. Owing to this adaptability, the Einasto profile has been shown to reproduce the radial density distributions of simulated dark matter halos across a wide range of masses and cosmological conditions with remarkable precision [79]. Specifically, it requires that [69, 73, 80]

$$\rho(r) = \rho_e \exp \left[-2\alpha^{-1} \left(\left(\frac{r}{r_e} \right)^\alpha - 1 \right) \right], \quad (1)$$

where α is the shaping parameter, r_e is the virial radius characterized by the logarithmic slope $\frac{d \ln \rho}{d \ln r} = -2$, and ρ_e is the halo density measured at the virial radius r_e . This profile results in a Kerr-like metric in Boyer-Lindquist Coordinates of the following form

$$ds^2 = -\frac{\Delta(r) - a^2 \sin^2 \theta}{\Sigma(r, \theta)} dt^2 + \frac{\Sigma(r, \theta)}{\Delta(r)} dr^2 + \Sigma(r, \theta) d\theta^2 + \sin^2 \theta \left[a^2 + r^2 + \frac{a \sin^2 \theta (a^2 + r^2 - \Delta(r))}{\Sigma(r, \theta)} \right] d\phi^2 - \frac{2a \sin^2 \theta (a^2 + r^2 - \Delta(r))}{\Sigma(r, \theta)} dt d\phi, \quad (2)$$

where the metric functions Δ and Σ are given as follows [73]

$$\Sigma(r, \theta) = r^2 + a^2 \cos^2 \theta, \quad (3a)$$

$$\Delta(r) = r^2 g(r) - 2Mr + a^2, \quad (3b)$$

$$g(r) = \exp \left\{ -4\pi 2^{1-3/\alpha} e^{2/\alpha} \alpha^{3/\alpha-1} r_e^3 \rho_e \frac{1}{r} \Gamma \left(3/\alpha, 0, \frac{2}{\alpha} \left(\frac{r}{r_e} \right)^\alpha \right) \right\}, \quad (3c)$$

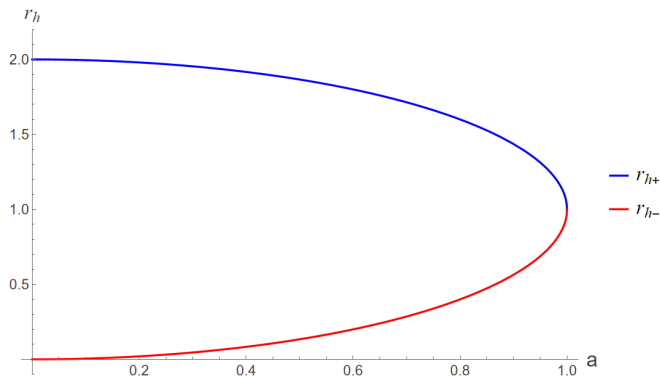


FIG. 1: Variation of the inner (r_{h-}) and outer (r_{h+}) horizons as a function of the black hole spin a . Note the derivative of both curves going to infinity at the intersection.

and Γ is the incomplete generalized Gamma function.

The multiplicative exponential term associated with r^2 introduces particularly interesting behavior in how the horizon structure depends on the halo parameters. Notably, setting the density parameter $\rho_e = 0$ naturally recovers the Kerr solution, without requiring adjustments to r_e or α . In the vicinity of the black hole, as $r/r_e \rightarrow 0$ ($r \ll r_e$), we find that $g(r) \approx e^{-\gamma r^2}$, where $\gamma = \frac{8\pi}{3} e^{2/\alpha}$. This result reflects the effectively Gaussian character of the dark matter distribution in the vicinity of the black hole, where its influence is minimal. On larger, intergalactic scales, however, the parameters α and r_e play a more significant role in shaping the overall halo profile as r increases. Within the immediate gravitational environment of the black hole, variations in α and r_e do not qualitatively alter the spacetime geometry, but instead modulate the degree to which changes in ρ_e affect the horizon structure. In this paper, unless otherwise stated, we adopt the dark matter halo parameters for the M87 galaxy as $\rho_e = 6.9E6M_\odot/kpc^3$, $r_e = 91.2kpc$ and $\alpha = 0.16$ [73], and convert ρ_e and r_e into black hole units ($M = 1$) for calculations in Eq. 3c using

$$r_e(\text{BHunits}) = r_e / (2GM_{\text{BH}}/c^2), \quad (4a)$$

$$\rho_e(\text{BHunits}) = \rho_e / (M_{\text{BH}} / (4/3\pi(2GM_{\text{BH}}/c^2)^3)). \quad (4b)$$

One particularly notable feature of this black hole arises under extreme parameter conditions. Our analysis primarily focuses on the spin parameter a and the dark matter density ρ_e . The spin exhibits an extremal value, denoted a_{extr} at which the outer (r_{h+}) and inner (r_{h-}) horizons coincide. At this critical point, the derivatives of the horizon radii with respect to spin diverge, $\frac{\partial r_{h+}}{\partial a} = \frac{\partial r_{h-}}{\partial a} = \infty$, as illustrated in Fig. 1. This behavior implies that the inverse derivative vanishes, $\left(\frac{\partial r_h}{\partial a}\right)^{-1} = 0$, where the merged horizon is expressed as a function $r_h(a_{\text{extr}}, M, \rho_e, r_e, \alpha)$. This allows us to use an implicit derivative method to find r'_h from the condition $\Delta(r_h) = 0$, and then explicitly solve for r_h and a_{extr} .

To investigate how variations in the dark matter density influence the black hole structure, we examine the dependence of a_{extr} and r_h on ρ_e , as shown in Fig. 2. As ρ_e increases, the

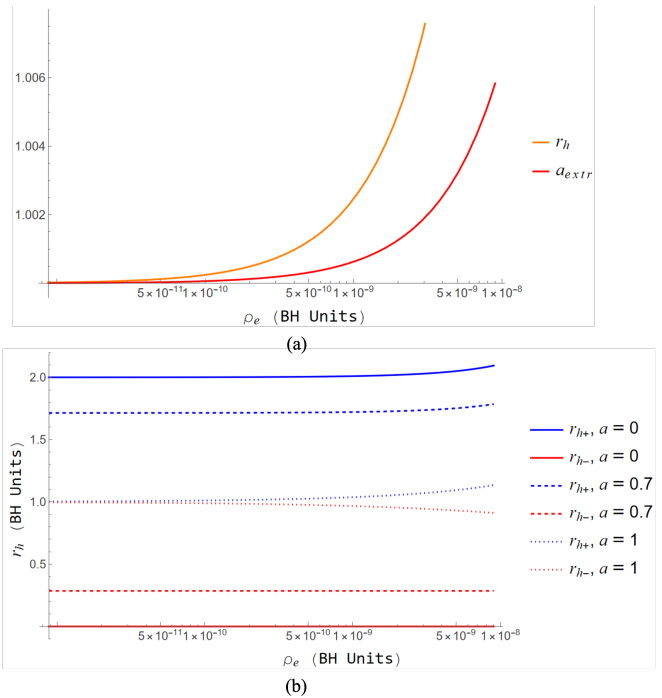


FIG. 2: Panel (a) shows r_h and a_{extr} with varying ρ_e ; and panel (b) shows r_{h+} and r_{h-} with varying ρ_e . Note that both graphs are on a horizontal log scale. Also, $\rho_e \in (0, 9E - 9]$ is scaled in BH units with $M = 1$.

outer event horizon expands, consistent with the expectation that additional surrounding mass effectively deepens the gravitational potential. A noteworthy consequence of this behavior is the corresponding increase in a_{extr} , indicating a broader range of allowable spin values than those predicted by the Kerr metric. In realistic astrophysical contexts, however, the dark matter density in the M87 galaxy has been estimated to be on the order of $O(10^{-21})$ in black hole units, several orders of magnitude below the densities at which this shift in the extremal spin becomes appreciable.

III. THE INCLUSION OF PLASMA IN GEOMETRICAL OPTICS IN CURVED SPACE-TIME

In this section, we consider a more realistic scenario where the black hole is surrounded by a light-dispersive medium such as plasma, where rays no longer follow light-like geodesics of the spacetime metric. We assume no interaction between the black hole spacetime and plasma, meaning that the parameters of the rotating black hole immersed in a dark matter halo remain unaffected by plasma properties. We work within the framework of geometric optics, where light propagation is described in terms of rays rather than waves. This approach simplifies the interaction between plasma and light by considering only how the plasma affects the trajectories of the rays. Here our focus is on studying the effect of a non-magnetized, pressureless plasma medium as

it has a unique property that its effect on light propagation is entirely determined by the plasma frequency $\omega_p(x)$. Starting with the Hamiltonian in vacuum

$$\mathcal{H} = \frac{1}{2} p_\mu p^\mu = \varepsilon, \quad (5)$$

where p_μ is the 4-momentum defined as $p_\mu = g_{\mu\nu} \dot{x}^\nu$ and $\varepsilon \in (-1, 0, 1)$ for time-like, light-like, and space-like particles, respectively. We then add the plasma contribution using the plasma frequency $\omega_p(x)^2 = \frac{e^2}{m} \hat{n}(x)$, where e is the electron charge, m is the mass of the electron, and $\hat{n}(x)$ is the electron density which is a function of our coordinates x [73, 81–85]. The Hamiltonian for light-like particles is now rewritten as

$$\mathcal{H} = \frac{1}{2} (p_\mu p^\mu + \omega_p(x)^2) = 0. \quad (6)$$

A. Introduction of the Index of Refraction

We proceed with the approach developed by Perlick and Tsupko in [81, 85] and rewrite the photon's 4-momenta p^μ relative to an observer in terms of its time-like four velocity $U^\mu(x)$:

$$p^\mu = -\omega(x)U^\mu(x) + k^\mu(x), \quad (7)$$

where $\omega(x) = p_\mu U^\mu(x)$ and $k^\mu(x) = p^\mu + p_\nu U^\nu(x)U^\mu(x)$ are the frequency and spatial wave vector of the light, respectively. The condition $\mathcal{H} = 0$ now becomes a dispersion relation

$$\omega(x)^2 = k_\mu(x)k^\mu(x) + \omega_p(x)^2, \quad (8)$$

which, due to $k^\mu(x)$ being spacelike, implies that $\omega(x)^2 \geq \omega_p(x)^2$. The index of refraction can be found by simplifying Eq. 8

$$n(x, \omega(x))^2 \equiv \frac{1}{v_p(x, \omega(x))^2} = \frac{k_\mu(x)k^\mu(x)}{\omega(x)^2} = 1 - \frac{\omega_p(x)^2}{\omega(x)^2}, \quad (9)$$

where $v_p(x, \omega(x))^2$ is the phase velocity.

With the introduction of the refractive index, we gain a clearer physical interpretation of how plasma influences light propagation. When the photon frequency satisfies $\omega(x) > \omega_p(x)$, the refractive index is real and nonzero, allowing light to propagate through the plasma. In contrast, when $\omega(x) < \omega_p(x)$, the refractive index becomes purely imaginary, corresponding to an absorptive medium through which light cannot propagate. This condition imposes an upper limit on the plasma frequency for which transmission remains possible at a given photon frequency. Beyond this limit, the plasma surrounding the black hole becomes opaque to the photon. For real values of the refractive index, however, the plasma acts as a dispersive medium, introducing an effective lensing of photon trajectories and thereby influencing the underlying geodesic structure.

B. Two Plasma Profiles

For Kerr spacetimes, it is well established in the literature [73, 81–85] that the plasma frequency has to take the following form:

$$\omega_p(r, \theta)^2 = \frac{f_r(r) + f_\theta(\theta)}{\Sigma(r, \theta)} \quad (10)$$

to allow analytically separable geodesic solutions (also explained later in Sec. IV A). In this paper, we focus on studying two particular profiles of homogeneous and inhomogeneous plasma. For the homogeneous plasma case, we define

$$f_{r(Homo)}(r) = \omega_c^2 r^2, \quad (11a)$$

$$f_{\theta(Homo)}(\theta) = \omega_c^2 a^2 \sin^2 \theta, \quad (11b)$$

where ω_c is the fundamental plasma frequency defined by $\omega_c^2 = \frac{e^2}{m} \hat{n}$ and \hat{n} represents a uniform electron density. The advantage of adopting a homogeneous plasma profile is twofold. First, it still permits variation of the refractive index as a function of r and θ , since photons experience gravitational redshift while propagating through the curved spacetime [81]. Second, it enables an intuitive interpretation of the parameter ω_c as an effective measure of plasma density, where larger (smaller) values of ω_c correspond to stronger (weaker) plasma effects, or equivalently, greater (lesser) “plasma strength.”

For the inhomogeneous plasma profile, we adopt the combination of the two plasma distributions discussed in [81] and define

$$f_{r(Inhomo)}(r) = \omega_c^2 \sqrt{M^3 r}, \quad (12a)$$

$$f_{\theta(Inhomo)}(\theta) = \omega_c^2 M^2 (1 + 2 \sin^2 \theta), \quad (12b)$$

where M is the black hole mass and set to unity in black hole units. While this configuration does not represent the most complex or fully realistic plasma environment, it offers a valuable balance between physical relevance and analytical clarity. Our preliminary analysis showed that the two plasma models yield qualitatively consistent behaviors, differing mainly in the magnitude of their effects. By combining them, we enhance the visibility of plasma-induced phenomena and achieve a clearer comparison among the three cases considered: no plasma, inhomogeneous plasma, and homogeneous plasma. Moreover, this approach naturally introduces explicit dependence on both r and θ , aligning well with the spatial variations typically seen in GRMHD simulations [86, 87].

IV. NULL GEODESICS AND GRAVITATIONAL LENSING

A. Plasma Influence on Photon Orbits

To further study the impact of plasma on null geodesics, we assume the following separable action ansatz [73, 81, 82, 88]

$$S = -Et + L_z \phi + S_r(r) + S_\theta(\theta), \quad (13)$$

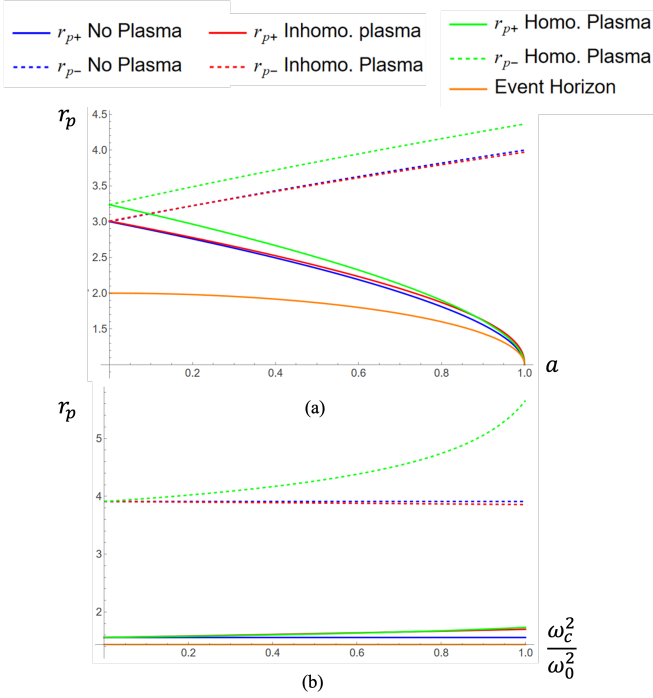


FIG. 3: Panel (a) shows the variation of r_{p+} and r_{p-} as a function of a for different plasma models, while ω_c^2/ω_0^2 is kept at 0.5; Panel (b) shows the variation of r_{p+} and r_{p-} as a function of ω_c^2/ω_0^2 for different plasma models, while a is kept at 0.99.

where E and L_z are the conserved energy and azimuthal angular momentum per unit mass at infinity, respectively, and $S_r(r)$, $S_\theta(\theta)$ are separated actions in terms of r , θ , respectively. Plugging this ansatz into Eq. 6 with $p_\mu = \frac{\partial S}{\partial x^\mu}$, we get

$$g^{\mu\nu} \frac{\partial S}{\partial x^\mu} \frac{\partial S}{\partial x^\nu} + \omega_p(x)^2 = \Delta(r) \frac{\partial S_r(r)^2}{\partial r} + \frac{\partial S_\theta \theta^2}{\partial \theta} + (L_z \csc \theta - aE \sin \theta)^2 - \frac{((r^2 + a^2)E - aL_z)^2}{\Delta(r)} + \Sigma(r, \theta) \omega_p(x)^2 = 0. \quad (14)$$

Clearly, for the above equation to be analytically separable $\omega_p(x)$ must take the form

$$\omega_p(r, \theta)^2 = \frac{f_r(r) + f_\theta(\theta)}{\Sigma(r, \theta)}, \quad (15)$$

which leads to the following separated equations

$$\frac{\partial S_\theta \theta^2}{\partial \theta} + (L_z \csc \theta - aE \sin \theta)^2 + f_\theta(\theta) = -\Delta(r) \frac{\partial S_r(r)^2}{\partial r} + \frac{((r^2 + a^2)E - aL_z)^2}{\Delta(r)} - f_r(r). \quad (16)$$

By introducing the Carter constant κ and solving for the momenta, we obtain

$$\frac{\partial S_\theta \theta}{\partial \theta} = \sqrt{\Theta(\theta)} \quad (17a)$$

$$= \sqrt{\kappa - (L_z \csc \theta - aE \sin \theta)^2 - f_\theta(\theta)}, \quad (17b)$$

$$\Delta(r) \frac{\partial S_r(r)}{\partial r} = \sqrt{R(r)} \quad (17c)$$

$$= \sqrt{((r^2 + a^2)E - aL_z)^2 - \Delta(r)(\kappa + f_r(r))}. \quad (17d)$$

Now, using definitions $\frac{\partial S_r(r)}{\partial r} = p_r = g_{rr} \dot{r} = \frac{\Sigma(r, \theta)}{\Delta(r)} \dot{r}$ and $\frac{\partial S_\theta \theta}{\partial \theta} = p_\theta = g_{\theta\theta} \dot{\theta} = \Sigma(r, \theta) \dot{\theta}$, the final spherical geodesics equations are given by

$$\left(\frac{\Sigma(r, \theta)}{E} \right)^2 \dot{\theta}^2 = \frac{\Theta(\theta)}{E^2} = \chi - (\eta \csc \theta - a \sin \theta)^2 - \tilde{f}_\theta(\theta), \quad (18a)$$

$$\left(\frac{\Sigma(r, \theta)}{E} \right)^2 \dot{r}^2 = \frac{R(r)}{E^2} = (r^2 + a^2 - a\eta)^2 - \Delta(r)(\chi + \tilde{f}_r(r)), \quad (18b)$$

where $\tilde{f}_r(r) = \frac{f_r(r)}{E^2}$ and $\tilde{f}_\theta(\theta) = \frac{f_\theta(\theta)}{E^2}$. The impact parameters $\eta = \frac{L_z}{E}$ and $\chi = \frac{\kappa}{E^2}$ introduced here can be thought of as ϕ and θ angular momentum conservation constants. Since the energy of a photon measured at infinity is $E = \hbar\omega_0 = \omega_0$, where ω_0 is the frequency of the photon at infinity, $\tilde{f}_r(r)$ and $\tilde{f}_\theta(\theta)$ both include a $\frac{\omega_c^2}{\omega_0^2}$ factor, which we refer to as the analogous plasma density. To find the stable spherical photon orbits, we require $R(r_p) = 0$ and $\frac{dR(r_p)}{dr} = 0$, i.e.

$$4r_p(a^2 + r_p^2 - a\eta) - \Delta'(r_p)(\chi + \tilde{f}_r(r_p)) - \Delta(r_p)\tilde{f}_r'(r_p) = 0. \quad (19)$$

Solving this system of equations for η , χ in terms of r_p and enforcing a positive $\Theta(\theta)$, we get

$$\eta = \frac{1}{a^2 \Delta'(r_p)} \left(a(a^2 + r_p^2) \Delta'(r_p) - 2ar_p \Delta(r_p) - 2\sqrt{a^2 \Delta(r_p)^2 r_p^2} \right), \quad (20a)$$

$$\chi = \frac{1}{a \Delta'(r_p)^2} (8ar_p^2 \Delta(r_p) + 8ar_p^2 \Delta(r_p)). \quad (20b)$$

The radial range of the asymptotically stable photon sphere is bounded by the equatorial plane co- and counter-rotating circular orbits [73, 81, 82, 89, 90]. By setting $\theta = \pi/2$, we obtain $R(r)$ at the equatorial plane

$$\left(\frac{\Sigma(r, \theta)}{E} \right)^2 \dot{r}^2 = \frac{R(r)}{E^2} \quad (21)$$

$$= (r^2 + a^2 - a\eta)^2 - \Delta(r) \left((\eta - a)^2 + \tilde{f}_\theta\left(\frac{\pi}{2}\right) + \tilde{f}_r(r) \right). \quad (22)$$

We numerically solve the above equation under the conditions $R(r) = \frac{dR(r)}{dr} = 0$ to obtain the co-rotating and

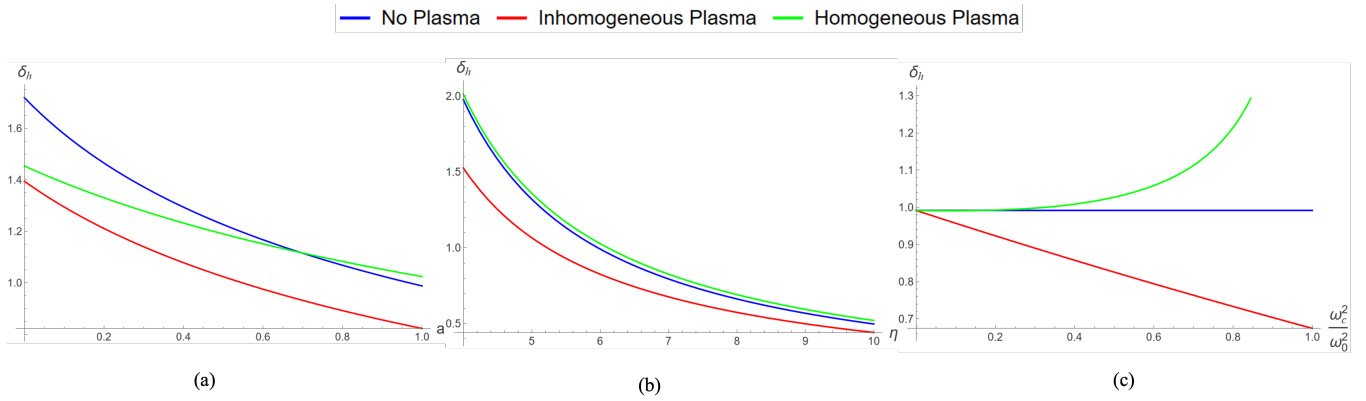


FIG. 4: Variations of deflection angle as a function of a (Panel (a)), η (Panel (b)), and ω_c^2/ω_0^2 (Panel (c)) for different plasma models. In all cases, $\rho_e = 6.9E6M_\odot/kpc^3$, $r_e = 91.2kpc$, and $\alpha = .16$

counter-rotating photon orbits. Fig. 3 illustrates how these orbital radii vary with the black hole spin a and plasma density $\frac{\omega_c^2}{\omega_0^2}$. In panel (a) of Fig. 3, as the spin increases, all plasma models exhibit the expected co-rotating limiting behavior consistent with the Kerr solution, where for unit mass $r_{p+} \rightarrow 1$ as $a \rightarrow 1$, ultimately merging with the event horizon. However, unlike the Kerr case, where $r_{p-} \rightarrow 4$ for the counter-rotating orbit as $a \rightarrow 1$, our results show distinct variations among the different plasma configurations. In particular, the homogeneous plasma solution generally yields larger photon orbit radii than both the inhomogeneous plasma and vacuum (no plasma) cases, while the inhomogeneous plasma solution produces slightly smaller counter-rotating and slightly larger co-rotating orbits. This trend can be understood from panel (b) of Fig. 3, which shows that the counter-rotating photon orbit radius increases exponentially with plasma density in the homogeneous case, whereas it decreases approximately linearly in the inhomogeneous case. For both plasma models, the co-rotating photon orbit radius increases with plasma density, moving progressively outward from the event horizon and away from the corresponding vacuum (no plasma) orbit.

B. Plasma Influence on Deflection Angle

Next, we evaluate the deflection angle of photons with a given impact parameter (η, χ) . This angle serves as a measure of the gravitational lensing produced by the black hole. Although this calculation does not constitute a complete reconstruction of the resulting lensed image, it provides valuable insight into the behavior of light rays in the vicinity of the black hole and serves as a useful diagnostic for probing spacetime curvature and plasma effects. The deflection angle δ_h is given by

$$\delta_h + \pi = \int_{R_c}^{\infty} \frac{d\phi}{dr} \Big|_{\theta_0} dr, \quad (23)$$

where R_c is the radius of closest approach. Applying Hamilton's equations $\dot{x}^\mu = \frac{\partial \mathcal{H}}{\partial x^\mu}$, we get:

$$\begin{aligned} \delta_h + \pi &= \int_{R_c}^{\infty} \frac{d\phi}{dr} dr \\ &= \int_{R_c}^{\infty} \frac{\frac{a}{\Delta(r)} [(r^2 + a^2) - a\eta] + \eta \csc^2 \theta - a}{\pm \sqrt{(r^2 + a^2 - a\eta)^2 - \Delta(r) (\chi + \tilde{f}_r(r))}} \Big|_{\theta_0} dr. \end{aligned} \quad (24)$$

Here, χ can be solved uniquely from $\Theta(\theta) = 0$ for any given θ_0 , which results in

$$\chi = -(\eta \csc \theta_0 - a \sin \theta_0)^2 + \tilde{f}_\theta(\theta_0). \quad (25)$$

Thus, our final equation is

$$\begin{aligned} \delta_h + \pi &= \int_{R_c}^{\infty} \frac{d\phi}{dr} dr \\ &= 2 \int_{R_c}^{\infty} \frac{\frac{a}{\Delta(r)} M(r) + \eta \csc^2 \theta - a}{\sqrt{M(r)^2 - \Delta(r) (-(\eta \csc \theta - a \sin \theta)^2 + \tilde{f}_\theta(\theta) + \tilde{f}_r(r))}} \Big|_{\theta_0} dr, \end{aligned} \quad (26)$$

where the factor of 2 is due to the \pm in the denominator and the substitution $M(r) = r^2 + a^2 - a\eta$ is done for brevity.

We numerically compute the deflection angle for varying black hole spin a , photon impact parameter η , and plasma density $\frac{\omega_c^2}{\omega_0^2}$, with the results shown in Fig. 4. As expected, the deflection angle decreases with increasing impact parameter η , consistent with the physical intuition that photons with larger impact parameters (or equivalently, higher angular momentum) experience weaker gravitational influence, analogous to hyperbolic trajectories in Newtonian or Keplerian dynamics. When varying the spin parameter a , however, distinct behaviors emerge across the different plasma models due to the presence of the $-\Delta(r)\tilde{f}_r(r)$ term in the denominator, which includes a $-a^2\tilde{f}_r(r)$ contribution that

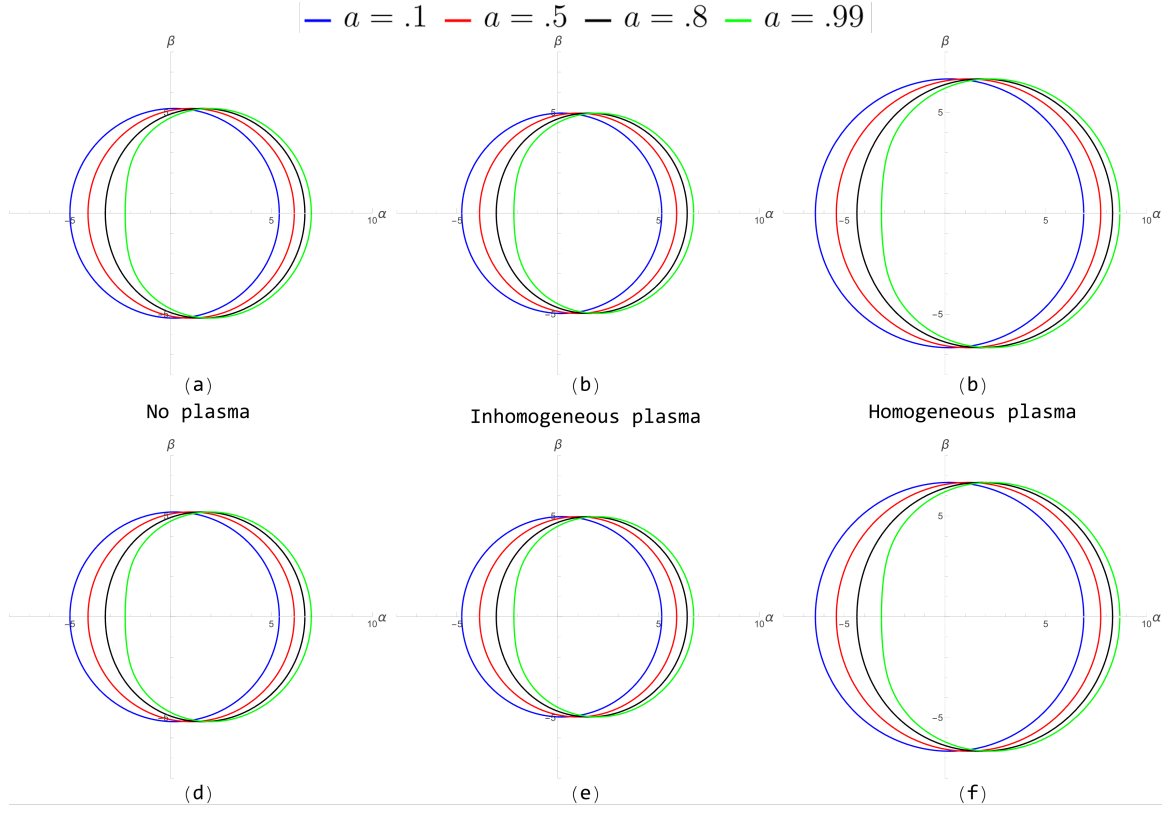


FIG. 5: Shadow shape for various values of black hole spin a and inclination angles θ_0 for no plasma, inhomogeneous plasma and homogeneous plasma profiles. Panels (a)-(c): $\theta_0 = \pi/2$; panels (d)-(f): $\theta_0 = \pi/12$. In all cases, $\rho_e = 6.9E6M_\odot/kpc^3$, $r_e = 91.2kpc$, $\alpha = .16$, and $\omega_c^2/\omega_0^2 = .5$

enhances the deflection angle. This effect is most pronounced for the homogeneous plasma model, where $\tilde{f}_r(r) \propto r^2$, resulting in a deflection angle that begins below the vacuum (no plasma) case but eventually exceeds it as a increases. In contrast, the inhomogeneous plasma model, characterized by $\tilde{f}_r(r) \propto \sqrt{r}$, exhibits a more moderate variation: although its deflection angle initially lies below the no-plasma case, it decreases more slowly with increasing spin, from roughly $\approx .25$ radians to $\approx .14$ radians, than in the vacuum scenario. This behavior becomes even clearer when varying $\frac{\omega_c^2}{\omega_0^2}$: increasing the homogeneous plasma strength enhances the deflection angle approximately exponentially, whereas increasing the inhomogeneous plasma strength reduces it in a near-linear fashion over the range plotted.

V. SHADOW AND OBSERVABLES ANALYSIS

A. Plasma Influence on Shadow

In this section, we set up celestial coordinates of the black hole shadow using Bardeen's dimensional coordinates [90], as also recently used in [73, 82, 89]. These coordinates are defined on a plane whose normal is perpendicular to the axis

of symmetry and oriented in the same azimuthal angle ϕ as the observer, and can be expressed as follows

$$\alpha = \lim_{r_0 \rightarrow \infty} -r_0^2 \sin \theta_0 \left(\frac{\partial \phi}{\partial r} \right) \Big|_{r_0, \theta_0}, \quad (27a)$$

$$\beta = \lim_{r_0 \rightarrow \infty} r_0^2 \left(\frac{\partial \theta}{\partial r} \right) \Big|_{r_0, \theta_0}. \quad (27b)$$

Applying Hamilton's equations $x^\mu = \frac{\partial \mathcal{H}}{\partial p_\mu}$, we get

$$\alpha = \lim_{r_0 \rightarrow \infty} -r_0^2 \sin \theta_0 \left(\frac{\frac{a}{\Delta(r_0)} [(r_0^2 + a^2) - a\eta] + \eta \csc^2 \theta_0 - a}{\sqrt{(r_0^2 + a^2 - a\eta)^2 - \Delta(r_0) (\chi + \tilde{f}_r(r_0))}} \right), \quad (28a)$$

$$\beta = \lim_{r_0 \rightarrow \infty} r_0^2 \left(\frac{\sqrt{\chi - (\eta \csc \theta_0 - a \sin \theta_0)^2 - \tilde{f}_\theta(\theta_0)}}{\sqrt{(r_0^2 + a^2 - a\eta)^2 - \Delta(r_0) (\chi + \tilde{f}_r(r_0))}} \right). \quad (28b)$$

Up until this point, this analysis has been agnostic of the form of $\Delta(r)$, $\tilde{f}_r(r_0)$, and $\tilde{f}_\theta(\theta_0)$; however, determining their leading-order behavior in r now becomes essential. From

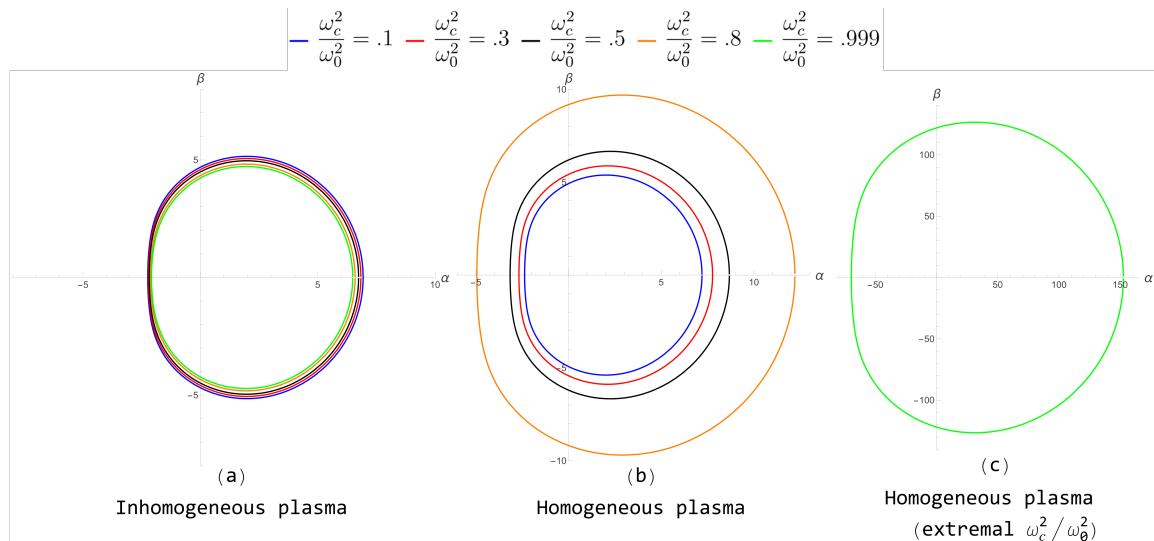


FIG. 6: Shadow shape for various values of ω_c^2/ω_0^2 for inhomogeneous plasma and homogeneous plasma profiles. In all cases, $a = 0.99$, $\rho_e = 6.9E6M_\odot/kpc^3$, $r_e = 91.2kpc$, $\alpha = .16$.

Eq. 28b, we note that the numerator scales as $O(r_0^2)$, implying that for the limit $r_0 \rightarrow \infty$ to remain finite, the denominator (i.e., $\sqrt{R(r_0)}$) must also scale as $O(r_0^2)$. This condition is satisfied if $\Delta(r_0)\tilde{f}_r(r_0) = O(r_0^4)$. Since the metric function $\Delta(r_0)$ depends on $g(r_0)$ through $r_0^2g(r_0)$, and $\lim_{r_0 \rightarrow \infty} g(r_0) = 1$, the leading-order behavior of $\Delta(r_0)$ is $O(r_0^2)$, constraining $\tilde{f}_r(r_0)$ to at most $O(r_0^2)$. Also, considering $\tilde{f}_r(r_0) = \omega_c^2 r_0^2$, evaluating $\sqrt{R(r_0)}$ yields a factor of $\sqrt{1 - \omega_c^2}$. Putting this all together, we obtain the following limits for homogeneous and inhomogeneous/no plasma, respectively,

$$\alpha_{Homo} = \frac{\eta \csc \theta_0}{\sqrt{1 - \omega_c^2}}, \quad (29a)$$

$$\beta_{Homo} = \frac{\sqrt{\Theta(\theta_0)}}{\sqrt{1 - \omega_c^2}}, \quad (29b)$$

$$\alpha_{Inhomo} = \eta \csc \theta_0, \quad (30a)$$

$$\beta_{Inhomo} = \sqrt{\Theta(\theta_0)}. \quad (30b)$$

These relations allow us to vary the celestial coordinates with $r_p \in [r_{p+}, r_{p-}]$, corresponding to the range of the unstable spherical photon sphere bounded by the co- and counter-rotating photon orbits. This parameterization enables us to compute and visualize the resulting black hole shadow shapes, as illustrated in Fig. 5. We notice several interesting trends as the viewing angle and spin parameter a are varied. We observe no significant difference in the overall shadow size between the viewing angles $\theta = \frac{\pi}{2}$ and $\theta = \frac{\pi}{12}$ for both the vacuum and inhomogeneous plasma models, as shown in panels (a)-(b) and (d)-(e) of Fig. 5. The shadow deformation decreases as the observer moves away from the equatorial plane, resulting in a reduced shift toward the direction of rotation (positive a) and less flattening on the opposite side, or a more circular shape.

Additionally, for all plasma configurations, the degree of deformation increases with the black hole spin a ; higher-spin cases exhibit stronger asymmetry, consistent with previous findings for rotating black holes [73, 81, 82]. Comparing across plasma types, we find that the inhomogeneous plasma solution generally produces slightly smaller shadows than the vacuum case, while the homogeneous plasma leads to noticeably larger ones.

To further investigate plasma effects, we examine how increasing the plasma density ω_c^2/ω_0^2 influences the shadow morphology, as illustrated in Fig. 6. Panel (a) shows that, for the inhomogeneous plasma model, increasing plasma density leads to a gradual reduction in the overall shadow radius while leaving its deformation largely unchanged. This trend is consistent with the deflection angles shown in Fig. 4, where the inhomogeneous plasma produces uniformly weaker deflection compared to the other two cases, resulting in fewer photons being captured by the black hole and thus a smaller shadow. In contrast, panel (b) shows that the homogeneous plasma exhibits the opposite behavior: the shadow size increases dramatically with plasma strength. This arises from the scaling relation discussed in Sec. V A, where the celestial coordinates are multiplied by a factor of $1/\sqrt{1 - (\omega_c^2/\omega_0^2)}$. As $\omega_c^2/\omega_0^2 \rightarrow 1$, this factor diverges, producing a pronounced inflation in shadow size, as shown in Fig. 6(c).

B. Shadow Observables

Beyond the overall shape, several measurable quantities can be used to characterize the black hole shadow, including its radius, deformation, and ellipticity. The shadow can be approximated as a nearly circular contour with an effective radius R_s , while deviations from circularity are quantified by

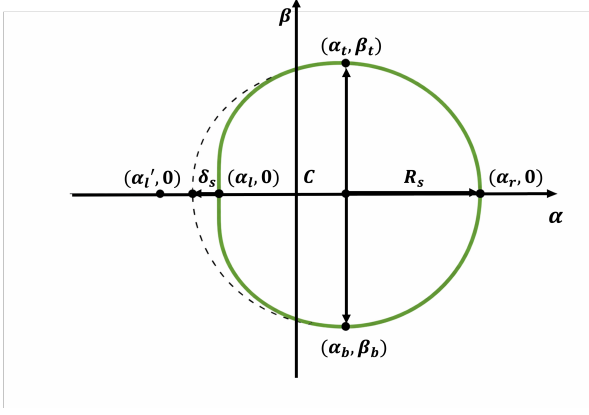


FIG. 7: Diagram of the shadow observables with relevant points labeled.

the flattening deformation δ_s and the ellipticity K_s , defined as the ratio of the vertical to horizontal widths. These quantities are derived from the characteristic points shown in Fig. 7, where the reference circle passing through the three points (α_t, β_t) , $(\alpha_r, 0)$, and (α_b, β_b) , defines the effective shadow radius R_s and the center position $(\alpha_c, 0)$:

$$R_s = \frac{(\alpha_r - \alpha_t)^2 + \beta_t^2}{2|\alpha_r - \alpha_t|}, \quad (31a)$$

$$\alpha_c = \frac{1}{2} \left(\alpha_r + \alpha_t + \frac{\beta_t}{-\alpha_r + \alpha_t} \right). \quad (31b)$$

We also make use of the reflectional symmetry of the Kerr-like shadow about the α -axis, which implies $(\alpha_b, \beta_b) = (\alpha_t, -\beta_t)$. Using this symmetry, the deformation parameter δ_s can be defined as the ratio between the deviation of the observed leftmost edge of the shadow from the reference circle and the effective shadow radius R_s . Specifically, it is given by the difference between the theoretical leftmost coordinate α'_l of the reference circle and the corresponding measured coordinate α_l of the Kerr-like shadow, normalized by R_s

$$\delta_s = \frac{\alpha_l - \alpha'_l}{R_s} = \frac{\alpha_l - (\alpha_c - R_s)}{R_s}. \quad (32)$$

And the ellipticity K_s , as stated above, is defined as the ratio of the horizontal width $\Delta\alpha$ and $\Delta\beta$:

$$K_s = \frac{\Delta\beta}{\Delta\alpha} = \frac{2\beta_t}{\alpha_r - \alpha_l}. \quad (33)$$

We first study the dependence of the shadow radius on the spin a , observer inclination angle θ_0 , plasma density ω_c^2/ω_0^2 , and dark matter density ρ_e , as illustrated in Fig. 8. We observe that the shadow size depends only weakly on spin (a slight growth of $\approx .07\%$) across all plasma models, but decreases gradually as the viewing angle θ_0 approaches its limits of 0 and π , as shown in panels (a)-(c) and (e), respectively. In addition, the plasma density ω_c^2/ω_0^2 affects the shadow radius differently depending on the plasma profile: the homogeneous plasma model produces an exponentially

increasing shadow radius relative to the vacuum case, whereas the inhomogeneous model shows an approximately linear decrease below the vacuum value, as illustrated in panel (f). We also explore the dependence of the shadow radius on the dark matter density ρ_e as we increase it from 10^{-34} to 10^{-9} in BH units in panel (d). Notice that the radius does not change significantly until $\rho_e > 10^{-11}$, where our values for M87* and Sgr A* are on the order of 10^{-21} and 10^{-28} in BH units respectively, which implies that for most physical dark matter densities there is no significant change in the shadow radius.

For the deformation δ_s and ellipticity K_s , panels (a) and (d) in Fig. 9 show that they both grow as the black hole spin a increases in nearly identical trends, consistent with the increasing flattening of the shadow observed at high spin in Fig. 5. Interestingly, the homogeneous plasma model remains closely aligned with the vacuum (no plasma) case, unlike the shadow radius behavior in Fig. 8, while the inhomogeneous plasma model shows a general decrease in both deformation and ellipticity with increasing spin. A similar pattern arises when varying the observer inclination angle θ_0 shown in panels (b) and (e): the homogeneous plasma case closely tracks the vacuum case, whereas the inhomogeneous plasma case produces smaller deformation and ellipticity values. As the viewing angle approaches its limits, the effects of plasma models on δ_s and K_s become indistinguishable, and the shadow becomes more circular. Finally, when varying the plasma density ω_c^2/ω_0^2 , panels (c) and (f) illustrate that the deformation δ_s and ellipticity K_s for the homogeneous plasma remain close to the vacuum case up to approximately $\omega_c^2/\omega_0^2 = .5$, beyond which they diverge exponentially. In contrast, δ_s and K_s for the inhomogeneous plasma decrease roughly linearly with increasing plasma density, consistent with its lower deformation and ellipticity values in the previous figures.

VI. ENERGY EMISSION RATE

The energy emission of black holes, most notably through Hawking radiation, arises from a process in which virtual particle pairs form near the event horizon, with one particle escaping to infinity while its partner falls inward, leading to a net loss of mass for the black hole. In this section, we are interested in investigating how various plasma profiles alter the energy emission rate in the spacetime of the Kerr-like black hole in a dark matter halo under consideration. The energy emission rate can be generally expressed as [91]

$$\frac{d^2 Z(\omega)}{d\omega dt} = \frac{2\pi\sigma_{lim}}{e^{T_H/\omega} - 1} \omega^3, \quad (34)$$

where σ_{lim} is the limiting constant, T_H is the Hawking temperature, and ω is the frequency. The limiting constant, which describes the effective area of the black hole shadow, can be expressed as

$$\sigma_{lim} = \frac{\pi^{\frac{d-2}{2}} R_s^{d-2}}{\Gamma(\frac{d}{2})}, \quad (35)$$

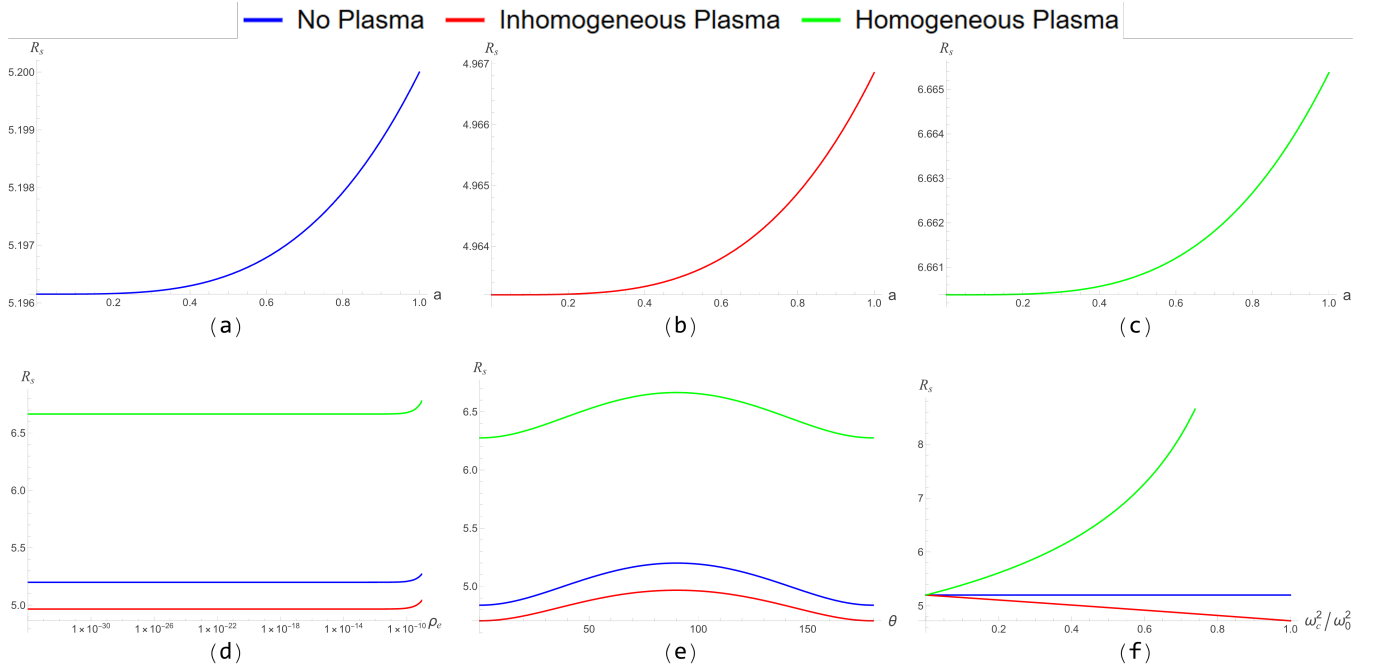


FIG. 8: Panels (a)-(c) show the variation of shadow radius R_s as a function of black hole spin a for different forms of plasma. We set $\theta_0 = \pi/2$, $\omega_c^2/\omega_0^2 = 0.5$, $\rho_e = 6.9E6M_\odot/kpc^3$, $r_e = 91.2kpc$, and $\alpha = .16$. Panel (d) shows the variation of shadow radius as a function of the log of the dark matter halo density ρ_e , while $\omega_c^2/\omega_0^2 = 0.5$, $\theta_0 = \pi/2$, and $a = 0.99$. Panel (e) shows the variation of shadow radius as a function of viewing angle θ , while $\theta_0 = \pi/2$ and $a = 0.99$. Panel (f) shows the variation of shadow radius as a function of ω_c^2/ω_0^2 , while $\theta_0 = \pi/2$ and $a = 0.99$.

where R_s is the effective radius of the shadow and d is the dimension. In $d = 4$ dimensions, we have

$$\sigma_{lim} = \pi R_s^2. \quad (36)$$

The Hawking temperature is given by [92]

$$T_H = \frac{\kappa}{2\pi}, \quad (37)$$

where κ is the surface gravity defined as in [93] using inner horizon r_{h-} , outer horizon r_{h+} and spin a :

$$\kappa = \frac{r_{h+} - r_{h-}}{2(r_{h+}^2 + a^2)}. \quad (38)$$

Fig. 10 shows the energy emission rate $\frac{d^2Z(\omega)}{d\omega dt}$ as a function of frequency ω for different plasma frequencies in the inhomogeneous and homogeneous plasma distributions. We see that for the inhomogeneous plasma model, the emission rate decreases as the plasma frequency increases, whereas in the homogeneous plasma model, it increases. We also compare the emission rates across plasma profiles with different plasma frequencies in Fig. 11. At low plasma frequency ($\omega_c^2/\omega_0^2 = 0.1$), the vacuum case produces the highest energy emission rate. The inhomogeneous plasma gives the lowest emission, with the homogeneous case falling in between. As the plasma frequency increases, the homogeneous plasma case has a much stronger effect, pushing

the emission rate higher compared to both the inhomogeneous plasma and no-plasma scenarios. At high plasma frequency ($\omega_c^2/\omega_0^2 = 0.7$), the inhomogeneous case exhibits a higher emission rate than the vacuum case. The change in ordering mirrors how each plasma profile modifies the shadow radius R_s , as we have seen in Fig. 8, which determines the effective area used in computing the energy emission rate.

VII. CONSTRAINTS FROM THE EHT OBSERVATIONAL DATA OF M87* AND Sgr A*

In 2019, the Event Horizon Telescope (EHT) collaboration released the first horizon-scale image of the supermassive black hole in the galaxy M87*, providing the first direct observational evidence of a black hole shadow [1]. This image revealed a bright emission ring surrounding a central intensity depression, whose angular diameter was shown to be consistent with the theoretical expectations for the shadow cast by a Kerr black hole. The observed ring size was inferred through model-dependent fits to the interferometric data and was found to be robust against variations in the underlying emission models. In 2022, the EHT collaboration reported the first image of the accretion flow surrounding Sgr A*, extending horizon-scale imaging to a second system with vastly different mass, accretion environment, and variability timescale [2, 94]. These observations provide a unique opportunity to test strong-gravity predictions across multiple

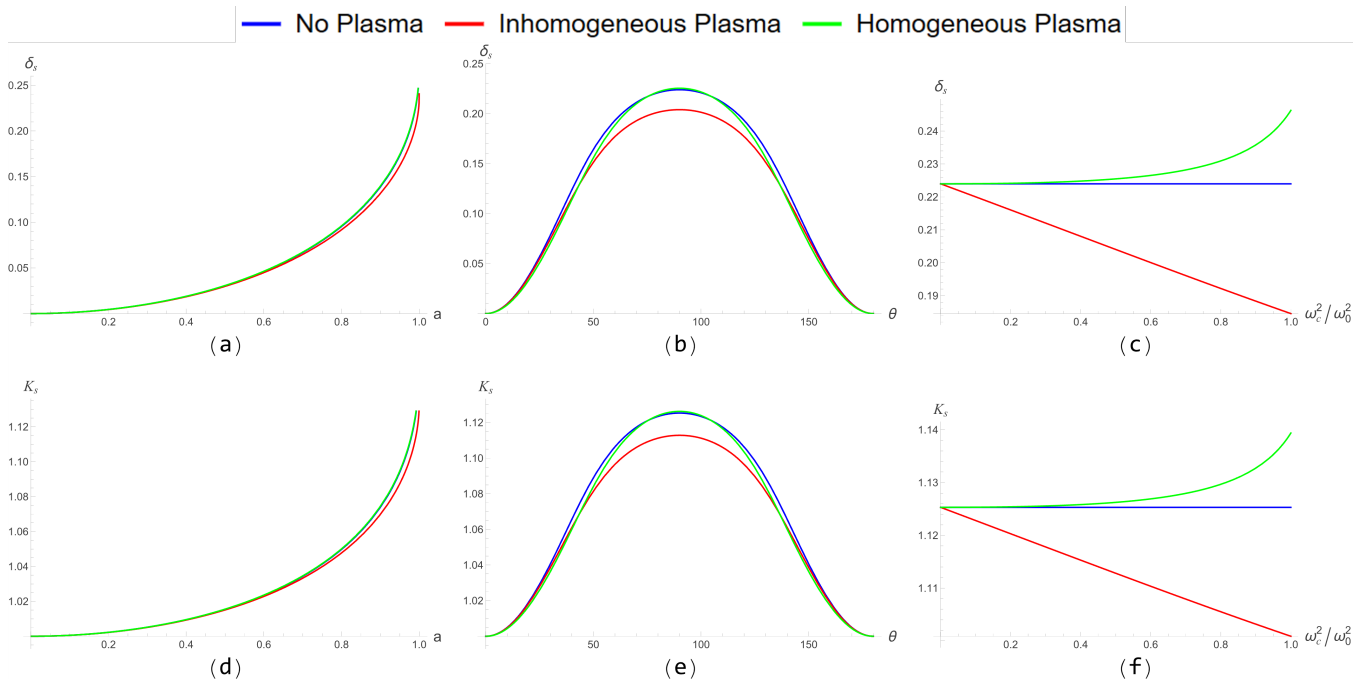


FIG. 9: Panels (a)-(c) show the variation of deformation δ_s as a function of black hole spin a , viewing angle θ and plasma frequency ω_c^2/ω_0^2 for different forms of plasma. Panels (d)-(f) show the variation of ellipticity K_s as a function of black hole spin a , viewing angle θ and plasma frequency ω_c^2/ω_0^2 for different forms of plasma. For Panels (a) and (d), we set $\theta_0 = \pi/2$, and $\omega_c^2/\omega_0^2 = 0.5$; for Panels (b) and (e), we set $a = 0.99$, and $\omega_c^2/\omega_0^2 = 0.5$; for Panels (c) and (f), we set $a = 0.99$, and $\theta_0 = \pi/2$.

astrophysical environments.

Rather than directly measuring a coordinate-dependent radius, the EHT constrains the apparent size of the black hole shadow on the observer's sky, which is determined by the lensing of light near unstable photon orbits. To facilitate comparisons with theoretical models and to minimize dependence on detailed shadow distortions, these constraints are commonly expressed in terms of an effective (areal) shadow radius, denoted r_{sh} . This quantity is defined through the total area A_{sh} enclosed by the shadow boundary as

$$r_{sh} \equiv \sqrt{\frac{A_{sh}}{\pi}}. \quad (39)$$

By construction, r_{sh} represents the radius of a circular disk with the same area as the observed shadow and provides a robust, model-independent characterization of the shadow size. Importantly, r_{sh} is an apparent celestial radius measured at infinity and should not be confused with the photon-sphere radius or any coordinate radius in the spacetime.

To compare different black hole systems, the shadow size is typically rendered dimensionless by normalizing with the black hole mass, r_{sh}/M , where M is expressed in geometric units. Observationally, this normalization is achieved by combining the measured angular shadow size with independent estimates of the black hole mass and distance, allowing the EHT to place constraints on r_{sh}/M that can be directly confronted with theoretical predictions.

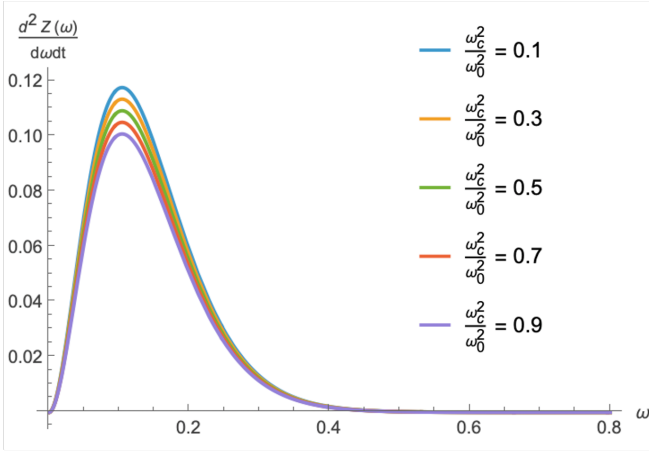
In practice, the shadow boundary extracted from ray-tracing simulations or observational reconstructions is not perfectly circular, especially for rotating black holes viewed at finite inclination. As a result, many studies characterize the shadow using its horizontal and vertical extents, defined respectively by

$$R_h = \frac{\alpha_r - \alpha_l}{2}, \quad R_v = \frac{\beta_t - \beta_b}{2}, \quad (40)$$

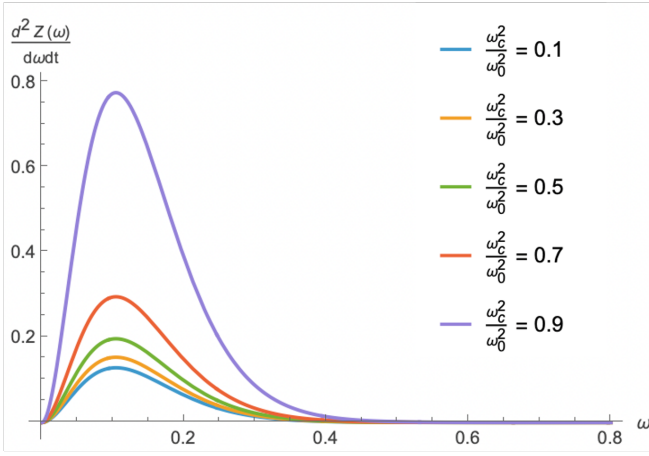
where $(\alpha_l, 0)$ and $(\alpha_r, 0)$ denote the leftmost and rightmost points of the shadow on the observer's screen, and $(0, \beta_t)$ and $(0, \beta_b)$ denote the top and bottom points. When the shadow is approximated as an ellipse with semi-axes R_h and R_v , its area may be written as $A_{sh} = \pi R_h R_v$, leading to the widely used approximation

$$r_{sh} \approx \sqrt{R_h R_v}. \quad (41)$$

This expression provides an efficient and accurate proxy for the areal shadow radius in Kerr-like spacetimes, with deviations typically at the percent level even for rapidly rotating black holes. Consequently, constraints on r_{sh}/M inferred by the EHT may be consistently compared with theoretical shadow calculations obtained from horizontal and vertical shadow radii, provided the definition of the effective shadow size is clearly stated. Based on the constraints derived and inferred by the EHT observations from the shadow image



(a)



(b)

FIG. 10: (a) Energy emission rate $\frac{d^2Z}{d\omega dt}$ as a function of frequency ω for inhomogeneous plasma; (b) Energy emission rate $\frac{d^2Z}{d\omega dt}$ as a function of frequency ω for homogeneous plasma. In both cases, $a = 0.5$, $\rho_e = 6.9E6M_\odot/kpc^3$, $r_e = 91.2kpc$, and $\alpha = .16$.

of Sgr A* and M87*, the range of the effective (areal) shadow radius r_{sh} should be within [95, 96]:

$$\text{Sgr A*} : \begin{cases} 4.55 \lesssim r_{sh}/M \lesssim 5.22 & (1\sigma) \\ 4.21 \lesssim r_{sh}/M \lesssim 5.56 & (2\sigma) \end{cases} \quad (42)$$

$$\text{M87*} : \begin{cases} 4.75 \lesssim r_{sh}/M \lesssim 6.25 & (1\sigma) \\ 4 \lesssim r_{sh}/M \lesssim 7 & (2\sigma) \end{cases} \quad (43)$$

Here σ represents the confidence level.

For Sgr A*, the relevant parameter are $M_{BH} = 4.297 \times 10^6 M_\odot$ [97], $r_e = 12kpc$, $\rho_e = 0.42 GeV cm^{-3} = 1.1 \times$

Plasma Profile	1σ	2σ
No Plasma	$0 < \frac{\omega_c^2}{\omega_0^2} < 1$	$0 < \frac{\omega_c^2}{\omega_0^2} < 1$
Inhomogeneous Plasma	$0 < \frac{\omega_c^2}{\omega_0^2} < 1$	$0 < \frac{\omega_c^2}{\omega_0^2} < 1$
Homogeneous Plasma	$0 < \frac{\omega_c^2}{\omega_0^2} < 0.1123$	$0 < \frac{\omega_c^2}{\omega_0^2} < 0.2593$

TABLE I: Allowed ranges of $\frac{\omega_c^2}{\omega_0^2}$ for different plasma profile based on Sgr A* data.

$10^7 M_\odot/kpc^3$ [98], $\theta_0 \approx \pi/2$, and $a = 0.9$ [99]. Table I and Figure 12 show the constraint of plasma densities based on the Sgr A* observation. For all types of plasma profile except the homogeneous one, the shadow radius is within the range of 2σ of the observation data. But since the radius increases significantly when homogeneous plasma densities increase, we found that the plasma densities have to be less than 0.2593 to fit into the observational range in 2σ confidence level.

Plasma Profile	1σ	2σ
No Plasma	$0 < \frac{\omega_c^2}{\omega_0^2} < 1$	$0 < \frac{\omega_c^2}{\omega_0^2} < 1$
Inhomogeneous	$0 < \frac{\omega_c^2}{\omega_0^2} < 1$	$0 < \frac{\omega_c^2}{\omega_0^2} < 1$
Homogeneous Plasma	$0 < \frac{\omega_c^2}{\omega_0^2} < 0.4274$	$0 < \frac{\omega_c^2}{\omega_0^2} < 0.5734$

TABLE II: Allowed ranges of $\frac{\omega_c^2}{\omega_0^2}$ for different plasma profiles based on M87* data.

For M87*, the relevant parameter are $M_{BH} = 6.5 \times 10^9 M_\odot$, $r_e = 91.2kpc$, $\rho_e = 6.9 \times 10^6 M_\odot/kpc^3$ and $\theta_0 = 17^\circ$ [73]. Table II and Figure 13 show the constraint of plasma densities based on the M87* observation. In the case of no plasma and inhomogeneous plasma, we observe that the radius matches the observed data for all plasma densities within the 1σ bound. For the homogeneous plasma, the plasma density needs to be less than 0.4274 to fit into the observational range in the 1σ confidence level, and 0.5734 for the 2σ confidence level. Overall, our analysis shows that the theoretical model under consideration is able to match the astrophysical observations under certain constraints of plasma densities.

VIII. DISCUSSION AND FUTURE WORK

In this paper, we explored how the shadow of Kerr-like black holes is influenced by the presence of plasma and surrounding dark matter halos. We first analyzed the horizon structure of a black hole embedded in a dark matter background and found that, for sufficiently large dark matter densities, both the extremal spin and horizon radius increase, reflecting an overall enhancement of the gravitational potential. Using Bardeen coordinates, we defined shadow observables (the shadow radius, deformation, and ellipticity) and compared our results with Event Horizon

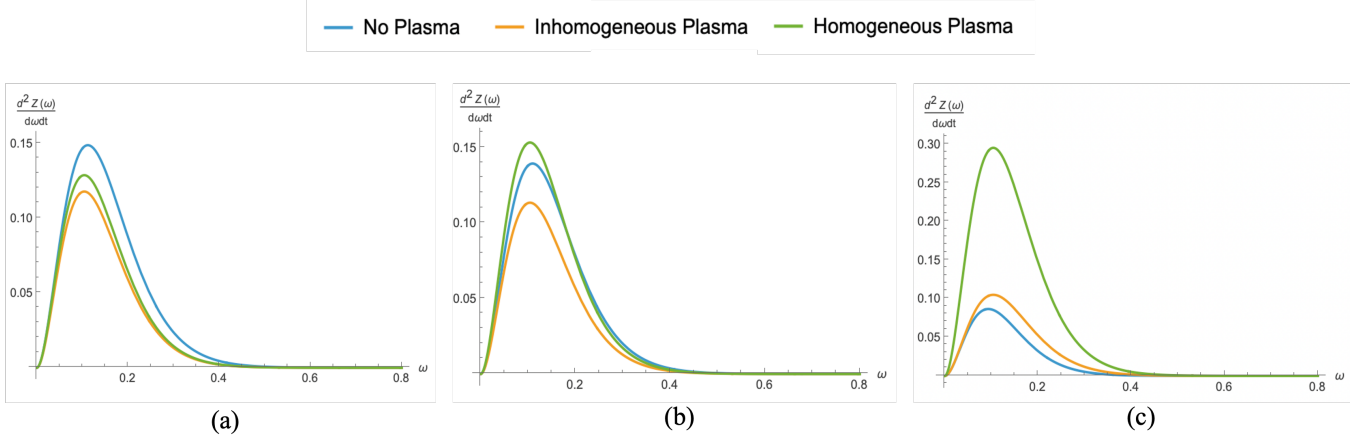


FIG. 11: Energy emission rate $\frac{d^2Z}{d\omega dt}$ as a function of frequency ω for different plasma profiles: (a) $\omega_c^2/\omega_0^2 = 0.1$; (b) $\omega_c^2/\omega_0^2 = 0.3$; (c) $\omega_c^2/\omega_0^2 = 0.7$. In all cases, $a = 0.5$, $\rho_e = 6.9E6M_\odot/kpc^3$, $r_e = 91.2kpc$, $\alpha = .16$.

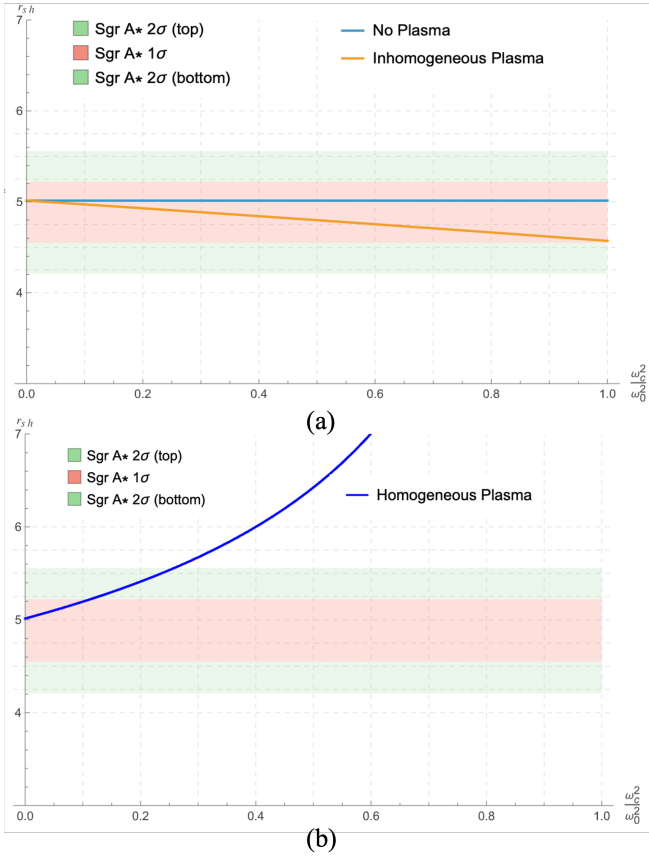


FIG. 12: Comparison of shadow radius for various plasma profiles to the observation of Sgr A*. Here, we set $a = 0.9$, $\rho_e = 1.1E7M_\odot/kpc^3$, $r_e = 12kpc$ and $\theta_0 \approx \pi/2$.

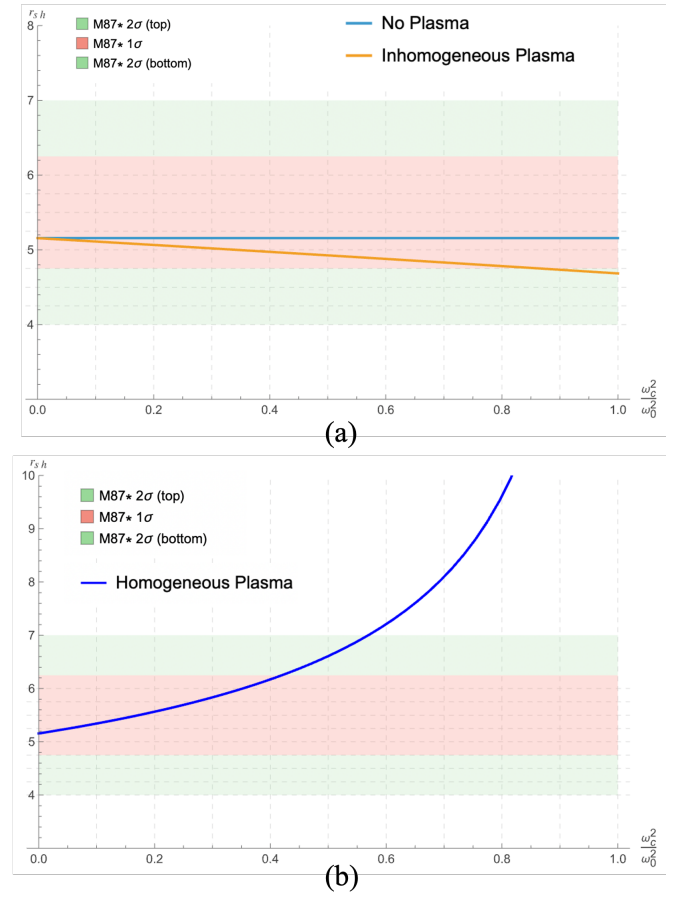


FIG. 13: Comparison of shadow radius of various plasma profiles to the observation of M87*. Here, we set $a = 0.5$, $\rho_e = 6.9E6M_\odot/kpc^3$, $r_e = 91.2kpc$, $\alpha = .16$ and $\theta_0 \approx 17^\circ$.

Telescope (EHT) measurements. We find that our theoretical models can fit within the 2σ bounds of the observed

shadow radii for both Sgr A* and M87* under certain

constraints. Although we modeled the dark matter halos using approximate parameters appropriate for each galaxy, their impact on the shadow observables is negligible. In contrast, we find a significant difference between homogeneous and inhomogeneous plasma distributions, with increasingly distinct behavior emerging as the plasma strength is increased.

Our present framework provides a controlled setting for exploring how plasma environments influence black hole shadow observables. The plasma models considered here are chosen to satisfy the common separability condition in Eq. 15, which enables analytic treatment and facilitates clear interpretation of qualitative trends. Within this class of models, we identify systematic differences between homogeneous and inhomogeneous plasma configurations. Extending this analysis to more general plasma distributions, potentially through numerical ray tracing or fully relativistic magnetohydrodynamic simulations, would be a natural direction for future work.

An interesting implication of these results is their relevance for interpreting EHT images of M87* and Sgr A* in

the presence of dust-like plasma in the interstellar and circumgalactic media [100, 101]. Such material is expected to modify photon propagation and can partially obscure the intrinsic black hole signal. The simplified plasma models employed here capture key qualitative features of these effects and may therefore serve as a useful starting point for developing more detailed correction schemes. While a quantitative determination of plasma parameters lies beyond the scope of the present study, the trends identified here may help inform future efforts aimed at constraining environmental contributions or mitigating their impact on black hole observables derived from EHT data.

ACKNOWLEDGMENTS

C. M. thanks the NSF LSAMP IINSPIRE Grant (NSF grant #2207350, subgrant #026450H) for funding this research. O. G., L. L., L.R. and S.R. acknowledge the support from the Grinnell College CSFS grant.

-
- [1] E. H. T. Collaboration, *Astrophysical Journal Letters* **875**, L1 (2019), [arXiv:1906.11238](#).
- [2] E. H. T. Collaboration, *Astrophysical Journal Letters* **930**, L12 (2022), [arXiv:2311.08697](#).
- [3] J. L. Synge, *Monthly Notices of the Royal Astronomical Society* **131**, 463 (1966).
- [4] J. M. Bardeen, in *Black Holes (Les Astres Occlus)*, edited by C. Dewitt and B. S. Dewitt (1973) pp. 215–239.
- [5] V. Perlick and O. Y. Tsupko, *Physical Review D* **90**, 104005 (2014), [arXiv:1409.4733](#).
- [6] V. Perlick (2000).
- [7] O. Y. Tsupko and G. S. Bisnovatyi-Kogan, *Phys. Rev. D* **87**, 124009 (2013).
- [8] V. Perlick, O. Y. Tsupko, and G. S. Bisnovatyi-Kogan, *Physical Review D* **92**, 104031 (2015), [arXiv:1507.04217](#).
- [9] V. Perlick and O. Y. Tsupko, *Physical Review D* **95**, 104003 (2017), [arXiv:1702.08768](#).
- [10] G. S. Bisnovatyi-Kogan and O. Y. Tsupko, *Grav. Cosmol.* **15**, 20 (2009), [arXiv:0809.1021 \[astro-ph\]](#).
- [11] G. S. Bisnovatyi-Kogan and O. Y. Tsupko, *Mon. Not. Roy. Astron. Soc.* **404**, 1790 (2010), [arXiv:1006.2321 \[astro-ph.CO\]](#).
- [12] X. Er and S. Mao, *Monthly Notices of the Royal Astronomical Society* **437**, 2180 (2014), [arXiv:1310.5825](#).
- [13] A. Rogers, *Mon. Not. Roy. Astron. Soc.* **451**, 17 (2015), [arXiv:1505.06790 \[gr-qc\]](#).
- [14] V. S. Morozova, B. J. Ahmedov, and A. A. Tursunov, *Astrophys. Space Sci.* **346**, 513 (2013).
- [15] F. Atamurotov and B. Ahmedov, *Phys. Rev. D* **92**, 084005 (2015), [arXiv:1507.08131 \[gr-qc\]](#).
- [16] A. Chowdhuri and A. Bhattacharyya, *Phys. Rev. D* **104**, 064039 (2021).
- [17] H. Yan, *Phys. Rev. D* **99**, 084050 (2019), [arXiv:1903.04382 \[gr-qc\]](#).
- [18] Z. Zhang, H. Yan, M. Guo, and B. Chen, *Phys. Rev. D* **107**, 024027 (2023), [arXiv:2206.04430 \[gr-qc\]](#).
- [19] M. Khodadi, *Nucl. Phys. B* **985**, 116014 (2022), [arXiv:2211.00300 \[gr-qc\]](#).
- [20] Y. Pahlavon, F. Atamurotov, K. Jusufi, M. Jamil, and A. Abdujabbarov, *Phys. Dark Univ.* **45**, 101543 (2024), [arXiv:2406.09431 \[gr-qc\]](#).
- [21] M. M. Gohain, K. Bhuyan, and P. Chutia, *Phys. Dark Univ.* **49**, 102064 (2025), [arXiv:2504.00581 \[hep-th\]](#).
- [22] X. Er and S. Mao, *Mon. Not. Roy. Astron. Soc.* **437**, 2180 (2014), [arXiv:1310.5825 \[astro-ph.CO\]](#).
- [23] G. S. Bisnovatyi-Kogan and O. Y. Tsupko, *Universe* **3**, 57 (2017), [arXiv:1905.06615 \[gr-qc\]](#).
- [24] C.-Q. Liu, C.-K. Ding, and J.-L. Jing, *Chin. Phys. Lett.* **34**, 090401 (2017), [arXiv:1610.02128 \[gr-qc\]](#).
- [25] G. Crisnejo and E. Gallo, *Phys. Rev. D* **97**, 124016 (2018), [arXiv:1804.05473 \[gr-qc\]](#).
- [26] G. Crisnejo, E. Gallo, and K. Jusufi, *Phys. Rev. D* **100**, 104045 (2019), [arXiv:1910.02030 \[gr-qc\]](#).
- [27] G. Crisnejo, E. Gallo, and A. Rogers, *Phys. Rev. D* **99**, 124001 (2019), [arXiv:1807.00724 \[gr-qc\]](#).
- [28] Y. Kumaran and A. Övgün, *Turk. J. Phys.* **45**, 247 (2021), [arXiv:2111.02805 \[gr-qc\]](#).
- [29] F. Atamurotov, A. Abdujabbarov, and J. Rayimbaev, *Eur. Phys. J. C* **81**, 118 (2021).
- [30] J. Sun, X. Er, and O. Y. Tsupko, *Mon. Not. Roy. Astron. Soc.* **520**, 994 (2023), [arXiv:2211.13442 \[astro-ph.SR\]](#).
- [31] G. S. Bisnovatyi-Kogan and O. Y. Tsupko, *Mon. Not. Roy. Astron. Soc.* **524**, 3060 (2023), [arXiv:2301.00053 \[gr-qc\]](#).
- [32] F. Feleppa, V. Bozza, and O. Y. Tsupko, *Phys. Rev. D* **110**, 064031 (2024), [arXiv:2406.07703 \[gr-qc\]](#).
- [33] A. Abdujabbarov, B. Toshmatov, Z. Stuchlík, and B. Ahmedov, *Int. J. Mod. Phys. D* **26**, 1750051 (2016), [arXiv:1512.05206 \[gr-qc\]](#).
- [34] Y. Huang, Y.-P. Dong, and D.-J. Liu, *Int. J. Mod. Phys. D* **27**, 1850114 (2018), [arXiv:1807.06268 \[gr-qc\]](#).
- [35] F. Atamurotov, K. Jusufi, M. Jamil, A. Abdujabbarov, and M. Azreg-Aïnou, *Phys. Rev. D* **104**, 064053 (2021), [arXiv:2109.08150 \[gr-qc\]](#).
- [36] A. Chowdhuri and A. Bhattacharyya, *Phys. Rev. D* **104**, 064039 (2021), [arXiv:2012.12914 \[gr-qc\]](#).
- [37] F. Ozel, D. Psaltis, and Z. Younsi, *Astrophys. J.* **941**, 88

- (2022), arXiv:2111.01123 [astro-ph.HE].
- [38] A. Das, A. Saha, and S. Gangopadhyay, *Class. Quant. Grav.* **39**, 075005 (2022), arXiv:2110.11704 [gr-qc].
- [39] J. Badía and E. F. Eiroa, *Phys. Rev. D* **107**, 124028 (2023), arXiv:2210.03081 [gr-qc].
- [40] A. Das, A. Saha, and S. Gangopadhyay, *Class. Quant. Grav.* **40**, 015008 (2023), arXiv:2207.06994 [gr-qc].
- [41] M. Fathi, M. Olivares, J. R. Villanueva, and N. Cruz, *Eur. Phys. J. Plus* **139**, 752 (2024), arXiv:2311.14017 [gr-qc].
- [42] M. A. Raza, M. Zubair, and E. Maqsood, *JCAP* **05**, 047 (2024), arXiv:2401.04779 [gr-qc].
- [43] R. Ali, X. Tiecheng, R. Babar, and A. Övgün, *Int. J. Theor. Phys.* **64**, 75 (2025), arXiv:2402.07657 [gr-qc].
- [44] R. Ali, X. Tiecheng, M. Awais, and R. Babar, *Chin. J. Phys.* **94**, 416 (2025), arXiv:2502.16273 [gr-qc].
- [45] S. Yasmin, K. Jafarzade, and M. Jamil, *Chin. Phys. C* **49**, 065107 (2025), arXiv:2502.18071 [gr-qc].
- [46] J. Badía and E. F. Eiroa, *Phys. Rev. D* **104**, 084055 (2021), arXiv:2106.07601 [gr-qc].
- [47] K. Akiyama *et al.* (Event Horizon Telescope), *Astrophys. J.* **912**, 35 (2021), arXiv:2105.01804 [astro-ph.HE].
- [48] G. Z. Babar, A. Z. Babar, and F. Atamurotov, *Eur. Phys. J. C* **80**, 761 (2020), [Erratum: *Eur.Phys.J.C* 82, 403 (2022)], arXiv:2008.05845 [gr-qc].
- [49] S. Kala and J. Singh, *Eur. Phys. J. C* **85**, 1047 (2025), arXiv:2507.17280 [gr-qc].
- [50] S. Kumar, A. Uniyal, and S. Chakrabarti, *Phys. Dark Univ.* **44**, 101472 (2024), arXiv:2403.12439 [gr-qc].
- [51] H. Feng, R.-J. Yang, and W.-Q. Chen, *Astropart. Phys.* **166**, 103075 (2025), arXiv:2403.18541 [gr-qc].
- [52] S. Kumar Sahoo and I. Banerjee, *JCAP* **10**, 100 (2025), arXiv:2504.09443 [gr-qc].
- [53] V. Perlick and O. Y. Tsupko, *Physics Reports* **947**, 1 (2022), arXiv:2105.07101.
- [54] V. C. Rubin, N. Thonnard, and W. K. Ford, Jr., *Astrophys. J.* **238**, 471 (1980).
- [55] M. Persic, P. Salucci, and F. Stel, *Mon. Not. Roy. Astron. Soc.* **281**, 27 (1996), arXiv:astro-ph/9506004.
- [56] G. Bertone, D. Hooper, and J. Silk, *Phys. Rept.* **405**, 279 (2005), arXiv:hep-ph/0404175.
- [57] D. Clowe, M. Bradac, A. H. Gonzalez, M. Markevitch, S. W. Randall, C. Jones, and D. Zaritsky, *Astrophys. J. Lett.* **648**, L109 (2006), arXiv:astro-ph/0608407.
- [58] G. Bertone and D. Hooper, *Rev. Mod. Phys.* **90**, 045002 (2018), arXiv:1605.04909 [astro-ph.CO].
- [59] P. Gondolo and J. Silk, *Phys. Rev. Lett.* **83**, 1719 (1999).
- [60] O. A. Hannuksela, K. C. Y. Ng, and T. G. F. Li, *Phys. Rev. D* **102**, 103022 (2020).
- [61] S. Peirani and J. A. de Freitas Pacheco, *Phys. Rev. D* **77**, 064023 (2008).
- [62] J. F. Navarro, C. S. Frenk, and S. D. M. White, *Astrophysical Journal* **462**, 563 (1996).
- [63] J. F. Navarro, C. S. Frenk, and S. D. M. White, *Astrophysical Journal* **490**, 493 (1997).
- [64] W. Dehnen, *Mon. Not. Roy. Astron. Soc.* **265**, 250 (1993).
- [65] M. M. Gohain, P. Phukon, and K. Bhuyan, *Phys. Dark Univ.* **46**, 101683 (2024), arXiv:2407.02872 [gr-qc].
- [66] A. Al-Badawi, S. Shaymatov, and Y. Sekhmani, *JCAP* **02**, 014 (2025), arXiv:2411.01145 [gr-qc].
- [67] A. Burkert, *Astrophysical Journal Letters* **447**, L25 (1995).
- [68] J. Einasto, *Trudy Astrofizicheskogo Instituta Alma-Ata* **5**, 87 (1965).
- [69] M. Baes and G. Gentile, *Astronomy & Astrophysics* **665**, A136 (2022), arXiv:2208.12321.
- [70] L. Hernquist, *Astrophysical Journal* **356**, 359 (1990).
- [71] N. Dai, Y. Gong, Y. Zhao, and T. Jiang, *Phys. Rev. D* **110**, 084080 (2024), arXiv:2301.05088 [gr-qc].
- [72] K. Jusufi, M. Jamil, P. Salucci, T. Zhu, and S. Haroon, *Phys. Rev. D* **100**, 044012 (2019), arXiv:1905.11803 [physics.gen-ph].
- [73] D. Liu, Y. Yang, Z. Xu, and Z.-W. Long, *Eur. Phys. J. C* **84**, 136 (2024), arXiv:2307.13553 [gr-qc].
- [74] A. Al-Badawi and S. Shaymatov, *Chin. Phys. C* **49**, 055101 (2025), arXiv:2501.15397 [gr-qc].
- [75] Q.-Q. Liang, D. Liu, and Z.-W. Long, *Eur. Phys. J. C* **85**, 1107 (2025), arXiv:2505.15540 [gr-qc].
- [76] U. Uktamov, S. Shaymatov, B. Ahmedov, and C. Yuan, (2025), arXiv:2509.00460 [gr-qc].
- [77] S. V. M. C. B. Xavier, H. C. D. Lima Junior, and L. C. B. Crispino, *Phys. Rev. D* **107**, 064040 (2023).
- [78] J. Wang, S. Bose, C. S. Frenk, L. Gao, A. Jenkins, V. Springel, and S. D. M. White, *Nature* **585**, 39 (2020), arXiv:1911.09720 [astro-ph.CO].
- [79] J. Wang, S. Bose, C. S. Frenk, L. Gao, A. Jenkins, V. Springel, and S. D. M. White, *Nature* **585**, 39 (2020).
- [80] J. Einasto, *Trudy Astrofizicheskogo Instituta Alma-Ata* **5**, 87 (1965).
- [81] V. Perlick and O. Y. Tsupko, **95**, 104003 ().
- [82] A. Das, A. Saha, and S. Gangopadhyay, **39**, 075005.
- [83] V. Perlick, O. Y. Tsupko, and G. S. Bisnovatyi-Kogan, **92**, 104031.
- [84] A. Chowdhuri and A. Bhattacharyya, **104**, 064039, 2012.12914 [gr-qc].
- [85] A. Rogers, **451**, 17.
- [86] C. F. Gammie, J. C. McKinney, and G. Toth, *The Astrophysical Journal* **589**, 444 (2003).
- [87] The Event Horizon Telescope Collaboration, *The Astrophysical Journal Letters* **875**, L5 (2019).
- [88] B. Carter, **174**, 1559.
- [89] V. Perlick and O. Y. Tsupko, **947**, 1 ().
- [90] J. M. Bardeen, in *Black Holes (Les Astres Occlus)*, edited by C. Dewitt and B. S. Dewitt (1973) pp. 215–239.
- [91] A. Das, A. Saha, and S. Gangopadhyay, *The European Physical Journal C* **80**, 180 (2020).
- [92] D. N. Page, *New Journal of Physics* **7**, 203 (2005).
- [93] Y.-C. Chou, *Heliyon* **6**, e03336 (2020).
- [94] A. Ciurlo and M. R. Morris, *?Sagittarius A* – The Milky Way Supermassive Black Hole.?* (2025), version Number: 1.
- [95] P. Kocherlakota *et al.* (Event Horizon Telescope), *Phys. Rev. D* **103**, 104047 (2021), arXiv:2105.09343 [gr-qc].
- [96] K. Akiyama *et al.* (Event Horizon Telescope), *Astrophys. J. Lett.* **930**, L12 (2022), arXiv:2311.08680 [astro-ph.HE].
- [97] GRAVITY Collaboration, R. Abuter, N. Aymar, P. Amaro Seoane, A. Amorim, M. Bauböck, J. P. Berger, H. Bonnet, G. Bourdarot, W. Brandner, V. Cardoso, Y. Clénet, R. Davies, P. T. De Zeeuw, J. Dexter, A. Drescher, A. Eckart, F. Eisenhauer, H. Feuchtgruber, G. Finger, N. M. Förster Schreiber, A. Foschi, P. Garcia, F. Gao, Z. Gelles, E. Gendron, R. Genzel, S. Gillessen, M. Hartl, X. Haubois, F. Haussmann, G. Heiße, T. Henning, S. Hippler, M. Horrobin, L. Jochum, L. Jocou, A. Kaufer, P. Kervella, S. Lacour, V. Lapeyrère, J.-B. Le Bouquin, P. Léna, D. Lutz, F. Mang, N. More, T. Ott, T. Paumard, K. Perraut, G. Perrin, O. Pfuhl, S. Rabien, D. C. Ribeiro, M. Sadun Bordonì, S. Scheithauer, J. Shangguan, T. Shimizu, J. Stadler, O. Straub, C. Straubmeier, E. Sturm, L. J. Tacconi, F. Vincent, S. Von Fellenberg, F. Widmann, M. Wielgus, E. Wieprecht, E. Wozzirek, and J. Woillez, *Astronomy & Astrophysics*

- [677, L10 \(2023\)](#).
- [98] J. F. Acevedo, A. J. Reilly, and L. Santos-Olmsted, [?Dark Drag Around Sagittarius A*?](#) (2025), version Number: 1.
- [99] L. A. Sánchez, [The European Physical Journal C](#) **84**, 1056 (2024).
- [100] S. Mathur, NASA ADAP Proposal , 15 (2015).
- [101] A. Misiriotis, E. M. Xilouris, J. Papamastorakis, P. Boumis, and C. D. Goudis, [Astronomy & Astrophysics](#) **459**, 113 (2006).